JGR Atmospheres

RESEARCH ARTICLE
10.1029/2019JD031110

Moisture Sources for Wintertime Intense Precipitation Events Over the Three Snowy Subregions of the Tibetan Plateau

Tianpei Qiu[1], Wenyu Huang[1], Jonathon S. Wright[1], Yanluan Lin[1], Ping Lu[1], Xinsheng He[1], Zifan Yang[1], Wenhao Dong[2,3], Hui Lu[1], and Bin Wang[1,4]

[1]Ministry of Education Key Laboratory for Earth System Modeling, and Department of Earth System Science (DESS), Tsinghua University, Beijing, China, [2]Cooperative Programs for the Advancement of Earth System Science, University Corporation for Atmospheric Research, Boulder, CO, USA, [3]Geophysical Fluid Dynamics Laboratory, NOAA, Princeton, NJ, USA, [4]State Key Laboratory of Numerical Modeling for Atmospheric Sciences and Geophysical Fluid Dynamics (LASG), Institute of Atmospheric Physics (IAP), Chinese Academy of Sciences, Beijing, China

Abstract Wintertime intense precipitation events often lead to severe snow disasters. In this study, a Lagrangian approach is employed to examine the evaporative moisture sources for wintertime intense precipitation events over the three snowy subregions of the Tibetan Plateau (TP) during 1979–2016, including the western TP (WTP), south central TP (SCTP), and southeastern TP (SETP). More than 80.0% of the moisture for intense precipitation over each subregion originates from terrestrial areas. Although prevailing westerly winds dominate above the TP and its surrounding areas during winter, half of the precipitation over the three subregions is supplied by evaporation from the south (i.e., the Indian Peninsula). Specifically, evaporation from the Indian Peninsula contributes 68.0%, 65.0%, and 45.0% of the moisture for intense precipitation over the WTP, SCTP, and SETP, respectively. The two primary oceanic moisture source regions for intense precipitation are the Arabian Sea and the Bay of Bengal, playing complementary roles in supplying moisture. The relative contributions of the Arabian Sea to intense precipitation over the WTP, SCTP, and SETP are 9.2%, 6.9%, and 1.1%, while those of the Bay of Bengal are 1.1%, 12.1%, and 8.6%. Southerly winds downstream of a cyclonic anomaly over the Indian Peninsula are crucial for the low-level moisture transport from the south to the Himalayan foothills. Under the combined effects of orographic lifting and favorable large-scale circulation patterns, moisture ascends further into the three subregions. Changes in the position and intensity of the cyclonic anomaly are particularly crucial to facilitating moisture contributions from the key source regions.

Key Points:
- The Indian Peninsula plays a leading role in supplying moisture for intense precipitation over the snowy subregions of the Tibetan Plateau
- A cyclonic anomaly over the Indian Peninsula is crucial for northward lower-level moisture transport to the Himalayan foothills
- A cyclonic anomaly embedded in the subtropical jet favors the onset of intense precipitation events over each snowy subregion

Supporting Information:
- Supporting Information S1

Correspondence to:
W. Huang,
huangwenyu@mail.tsinghua.edu.cn

Citation:
Qiu, T., Huang, W., Wright, J. S., Lin, Y., Lu, P., He, X., et al. (2019). Moisture sources for wintertime intense precipitation events over the three snowy subregions of the Tibetan Plateau. *Journal of Geophysical Research: Atmospheres*, *124*, 12,708–12,725. https://doi.org/10.1029/2019JD031110

Received 1 JUN 2019
Accepted 17 NOV 2019
Accepted article online 25 NOV 2019
Published online 8 DEC 2019

1. Introduction

The Tibetan Plateau (TP), Earth's largest store of ice outside the polar regions (Qiu, 2008), contains widespread snow cover (Li et al., 2017; Pu & Xu, 2009; Pu et al., 2007) and a total glacial area of nearly 10^5 km^2 (Yao et al., 2012). Meltwater from these snow cover and glaciers provides the sources for nearly all major river systems in Asia, directly impacting the lives of more than 1.4 billion people (Bookhagen & Burbank, 2010; Immerzeel et al., 2010; Qin et al., 2006; Su et al., 2013; Tong et al., 2014). The high elevation of the TP (mean elevation exceeding 4,000 m), which is often associated with extremely low temperatures (well below 0 °C), favors the formation and maintenance of snow cover and glaciers (Chu et al., 2014; Lu et al., 2005). However, it is worth noting that the ultimate source for these snow cover and glaciers is the precipitation over the TP (Forsythe et al., 2017; Li et al., 2017; Qin et al., 2006; Wang et al., 2017). During summer, snow cover and glaciers form mainly in the western TP (Chu et al., 2014; Li et al., 2017; Pu & Xu, 2009; Pu et al., 2007), which is characterized by higher altitudes and lower temperatures than other areas of the TP. Meanwhile, the majority of precipitation and meltwater over the remaining areas (i.e., the central and eastern TP) are transformed into surface runoff (Kulkarni et al., 2002; Lu et al., 2005; Xu et al., 2008). In comparison, wintertime precipitation over the TP contributes much less of the annual precipitation (about 10%; Maussion et al., 2014; 2017; Wan et al., 2017; Wang et al., 2018). However, most of the wintertime precipitation is in the form of snow and can be easily stored in the cryosphere due to the much colder temperatures relative to the summer (Lang & Barros, 2004; Li et al., 2017; Qin et al., 2006; Shen et al., 2015; Tang et al., 2018). Wintertime precipitation over the TP thus plays an essential role in the mass balance of the TP cryosphere

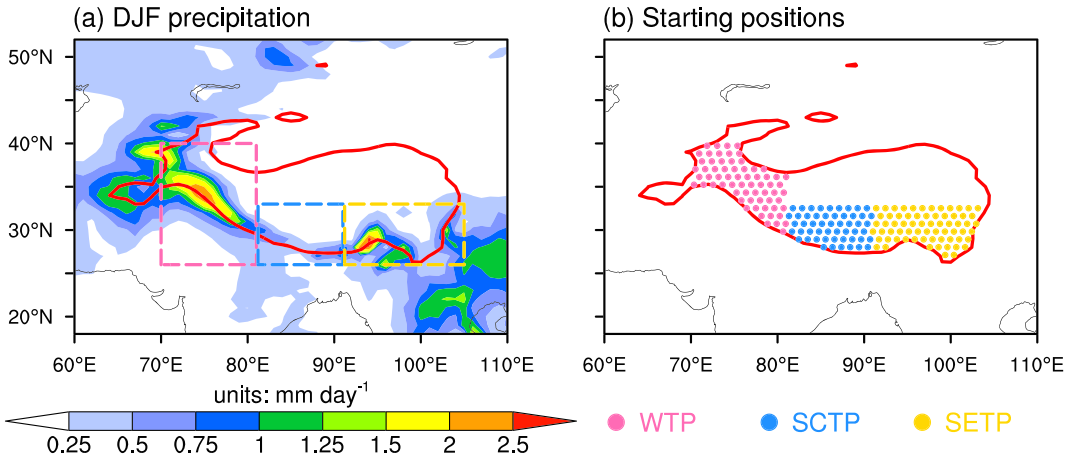

Figure 1. (a) Horizontal distribution of average precipitation (units: mm day^{-1}) over the Tibetan Plateau (TP) and its surrounding areas during DJF 1979–2016 based on ERA-Interim. (b) Horizontal distribution of the initial positions over the western TP (WTP; pink dots), south central TP (SCTP; blue dots), and southeastern TP (SETP; yellow dots). Regions bounded by solid red lines have surface altitudes higher than 2,500 m. The WTP, SCTP, and SETP are defined as the areas with surface altitudes exceeding 2,500 m within the pink dashed box (26–40°N, 70–81°E), blue dashed box (26–33°N, 82–91°E), and yellow dashed box (26–33°N, 92–105°E), respectively.

(Kulkarni et al., 2002; Lu et al., 2005; Smith & Bookhagen, 2018), and its formation mechanisms deserve thorough investigation.

Wintertime precipitation over the TP is mainly concentrated along the southern slope (Palazzi et al., 2013; Wang et al., 2018), including the western TP (WTP; Filippi et al., 2014; Liu et al., 2017; Shafiq et al., 2018; Syed et al., 2006), the south central TP (SCTP; Guo & Wang, 2014; Lang & Barros, 2004), and the southeastern TP (SETP; Liu et al., 2016; Pan et al., 2018; Sun & Wang, 2014). Notably, precipitation over the SCTP is slightly less than that over either the WTP or the SETP (Figure 1a). The occurrence of intense precipitation over the southern slope of the TP is closely related to the presence of an elevated region (i.e., the TP) under the subtropical westerly jet stream, which is conducive to orographic lifting (Curio & Scherer, 2016; Curio et al., 2015; Liu et al., 2017; Syed et al., 2006). Orographic lifting can in turn prompt convective ascent by lifting air parcels to their levels of free convection (Bonacina, 1945; Tucker, 2005). As a consequence, active convective systems can be observed over the southern slope of TP (Kurosaki & Kimura, 2002; Masafumi & Kenji, 2005; Maussion et al., 2014). Both orographic and convective uplift favor the occurrence of precipitation over the southern TP (Tucker, 2005). In addition to these two lifting processes, further study has revealed that cyclonic systems moving along the subtropical westerly jet stream play an important role in triggering wintertime intense precipitation over the TP by strengthening large-scale moisture convergence and updrafts (Cannon et al., 2014, 2015, 2016; Dimri et al., 2015; Forsythe et al., 2017; Lang & Barros, 2004; Li et al., 2018).

Proximity to moisture sources may also explain the presence of high-intensity precipitation over the southern slope of the TP, as the three subregions over the southern slope are closer to the tropics than other regions of the TP are. Specific humidities in the tropics are usually much higher than those in middle and high latitudes. To examine the moisture supply for precipitation over a specific region, two approaches are widely used: Eulerian moisture budget analysis in conceptualizing the moisture budget equation and Lagrangian moisture attribution analysis in tracking moisture sources and sinks. These approaches have been successfully applied to study the moisture supply to the whole TP (Curio et al., 2015; Pan et al., 2018) or various subregions of the TP, including the WTP (An et al., 2017; Kitoh & Arakawa, 2016; Tiwari et al., 2017), SCTP (Guo & Wang, 2014), and SETP (Guo & Wang, 2014; Kitoh & Arakawa, 2016; Sun & Wang, 2014).

Using numerical results from a global atmospheric general circulation model with a 20-km grid, Kitoh and Arakawa (2016) conducted Eulerian moisture budget analyses for wintertime precipitation over the eastern TP and WTP during 1979–2003. They found that the importance of local evaporation is comparable to that of large-scale moisture convergence (i.e., external sources) over the eastern TP, while moisture convergence plays a leading role over the WTP. Moisture for precipitation over the eastern TP mainly comes through the

southern and eastern boundaries, while that for precipitation over the WTP mainly comes through the western boundary. Tiwari et al. (2017) also found that large-scale moisture convergence plays a leading role in supplying moisture for precipitation over the western Himalayas (within the WTP) during the life cycles of western disturbances during 1979–2017. Western disturbances are closely related to the occurrence of wintertime heavy precipitation events. Based on the High Asia Refined analysis, Curio et al. (2015) concluded that large-scale moisture convergence plays a dominant role in supplying moisture for wintertime precipitation over the TP. They further indicated that these external moisture sources are transported to the TP mainly through its western and southern boundaries. They emphasized that advective transport of cloud particles plays an indispensable role in the moisture budget over the WTP.

Sun and Wang (2014) used the Flexible Particle (FLEXPART) Lagrangian particle dispersion model to examine the moisture sources for wintertime precipitation over the eastern TP during 2000–2009. They found that evapotranspiration over areas of the Eurasian continent to the north and west of the eastern TP contributes about 45% of the moisture, while evapotranspiration over the Indian Peninsula contributes about 14%. By contrast, ocean evaporation only contributes about 5% of the moisture for wintertime precipitation over the eastern TP. A variation of the Lagrangian moisture attribution analysis method can be implemented by including a water tagging module in an atmospheric general circulation model. Using the Community Atmosphere Model Version 3 (CAM3) with an embedded water tagging module, An et al. (2017) found that the five most important moisture source regions for wintertime precipitation over the northwestern TP during 1961–2012 are, in descending order, the Indian Ocean, the Pacific Ocean, the South China Sea, the Atlantic Ocean, and local evapotranspiration. Using a water tagging module in CAM5.1, Pan et al. (2018) compared the moisture source regions for wintertime precipitation over the southern TP and northern TP during 1982–2014. They found that the three most important source regions for the southern TP are Africa (contributed $16.7 \pm 5.8\%$), the TP ($16.5 \pm 6.1\%$), and India ($15.9 \pm 7.0\%$), while those for the northern TP are Africa ($25.2 \pm 3.7\%$), the North Atlantic Ocean ($13.7 \pm 3.7\%$), and Europe ($12.9 \pm 3.0\%$).

As described above, previous studies have mainly examined the moisture sources for precipitation over different subregions of the TP during the whole winter season. However, wintertime intense precipitation events not only contribute the majority of wintertime precipitation over the TP but can also lead to severe snow disasters (Liu et al., 2014; Yin et al., 2017). Such disasters may result in grassland being covered by snow, leading to destruction of housing, disruption of transportation, and loss of livestock (Gao et al., 2008; Li et al., 2018; Qiu et al., 2018). For example, in a series of severe snowfall events during the period from October 1995 to March 1996, more than 550,000 livestock perished and more than 38,000 people suffered from frostbite and other disabilities (e.g., snow blindness). The direct economic losses resulting from this series of snowfall events amounted to 340 million Chinese Yuan. Such events illustrate the need to better characterize the moisture sources for wintertime intense precipitation events over the TP.

In this study, we focus on wintertime intense precipitation events over three subregions of the TP (see the geographic position in Figure 1a), including the WTP (26–40°N, 70–81°E), the SCTP (26–33°N, 82–91°E), and the SETP (26–33°N, 92–105°E). These subregions are all located along the southern periphery of the TP and associated with relatively larger precipitation intensities compared to other regions of the TP. Compared to Eulerian moisture budget analysis, the major advantage of the Lagrangian approach is that it identifies both moisture sources and sinks, thereby enabling the construction of a detailed source-receptor relationship for atmospheric water. We use a Lagrangian approach to determine the evaporative moisture sources for wintertime intense precipitation events over these three subregions. Given the geographic differences among these three subregions, a question arises: How similar are the moisture source distributions? During winter, prevailing winds over the TP are predominantly westerly, which are unfavorable for moisture transport from the relatively humid terrestrial and oceanic areas to the south. A second question arises: What are the characteristic trajectories along which moisture from the key moisture source regions is transported to these three subregions of the TP? Assuming characteristic trajectories can be identified, then a third question arises: What synoptic circulation patterns favor moisture transport from these key moisture source regions during intense precipitation events? The objective of this work is to answer the above three questions.

The layout of the rest of this paper is organized as follows: Section 2 describes the data used, the algorithm for defining wintertime intense precipitation events over the three subregions, and the Lagrangian approach for determining the evaporative moisture sources for precipitation. Section 3 briefly introduces the basic

characteristics of intense precipitation events over each of the three subregions and validates the precipitation estimates derived using the Lagrangian approach. Section 4 compares moisture source distributions for the three subregions during their respective intense precipitation events. Section 5 presents the characteristic trajectories linking the key moisture source regions to the three subregions of the TP. Section 6 analyzes the synoptic circulation patterns that favor moisture transport from the key moisture source regions to the three subregions. Section 7 discusses the roles of two different large-scale circulation factors in the formation of the wintertime intense precipitation events. Section 8 provides a summary and concluding remarks. This section also examines our results in the context of previous studies.

2. Data and Methods

2.1. Data

Considering the scarcity of surface meteorological stations over the TP, precipitation data with a temporal resolution of 12 hr from the European Centre for Medium-Range Weather Forecasts Interim reanalysis (ERA-Interim; Dee et al., 2011) are used in this study to identify wintertime intense precipitation events over the three subregions of the TP during winter months from 1979 to 2016. Here the winter months for a specific year refer to December of that year and January–February of the following year (DJF). Daily precipitation data from the Asian Precipitation-Highly Resolved Observational Data Integration Towards the Evaluation of Water Resources (APHRODITE; Yatagai et al., 2009) during DJF 1979–2006, the Tropical Rainfall Measurement Mission (TRMM; Huffman et al., 2007) during DJF 1998–2016, and the Global Precipitation Climatology Project (GPCP; Huffman et al., 2001) during DJF 1996–2016 are used for validation.

ERA-Interim horizontal winds, vertical velocities, temperatures, and specific humidities on 60 model η levels are used together with surface pressure as inputs of the LAGRangian ANalysis TOol (LAGRANTO; Sprenger & Wernli, 2015; Wernli & Davies, 1997), which calculates backward trajectories for air parcels above the three subregions of the TP. Horizontal winds, air temperature, specific humidity, and geopotential height on pressure levels, snowfall, and surface temperature from ERA-Interim are also used for further diagnostic analyses. The temporal resolutions of all reanalysis variables are 6 hr.

All variables from ERA-Interim are used on a latitude-longitude grid with a uniform resolution of 1°. We retain the original temporal resolutions of the variables when running the LAGRANTO model, but use daily averages of the variables when conducting other kinds of diagnostic analyses.

2.2. Identification of the Wintertime Intense Precipitation Events

For each subregion, wintertime intense precipitation events are defined based on the following three steps. First, daily precipitation over each subregion is calculated as area-averaged precipitation within this subregion with surface altitudes higher than 2,500 m. Second, we identify wintertime intense precipitation events for a specific subregion as those days with daily precipitation in this subregion exceeding the 95th percentile. The 95th percentiles of daily precipitation for the WTP, SCTP, and SETP are 3.2, 0.9, and 1.7 mm day^{-1}, respectively, during DJF 1979–2016. For each subregion, this definition selects 172 intense days. Third, we define an intense event as a period containing one or more consecutive intense precipitation days. One non-intense day is allowed to exist between any two intense days during an intense event. Applying the above two steps identifies 114, 117, and 109 intense precipitation events for WTP, SCTP, and SETP, respectively.

2.3. A Lagrangian Approach for Determining Evaporative Moisture Sources

Prior to the Lagrangian analysis, 10-day backward trajectories are tracked for air parcels over a specific subregion (i.e., the target locations) of the TP using version 2.0 of LAGRANTO. A 10-day backward calculation time is adopted for consistency with the atmospheric moisture residence time scale (about 8 days; Trenberth, 1998, 1999). Horizontally, the target locations of these air parcels are distributed equidistantly with a grid spacing of 100 km (not 1°). The horizontal distributions of the air parcels for the three subregions are displayed in Figure 1b. Vertically, the target locations of these air parcels are distributed uniformly in the atmosphere from the surface to 200 hPa with a vertical grid spacing of 40 hPa. Surface pressure, specific humidity, relative humidity, and vertical velocity along backward trajectories corresponding to each air parcel are recorded at an interval of 6 hr.

The Lagrangian approach used for determining the moisture sources for precipitation over each subregion of the TP was originally designed by Stohl and James (2004). The key principle of this approach is that geographical positions with moisture increases along the Lagrangian trajectory for an air parcel can be viewed

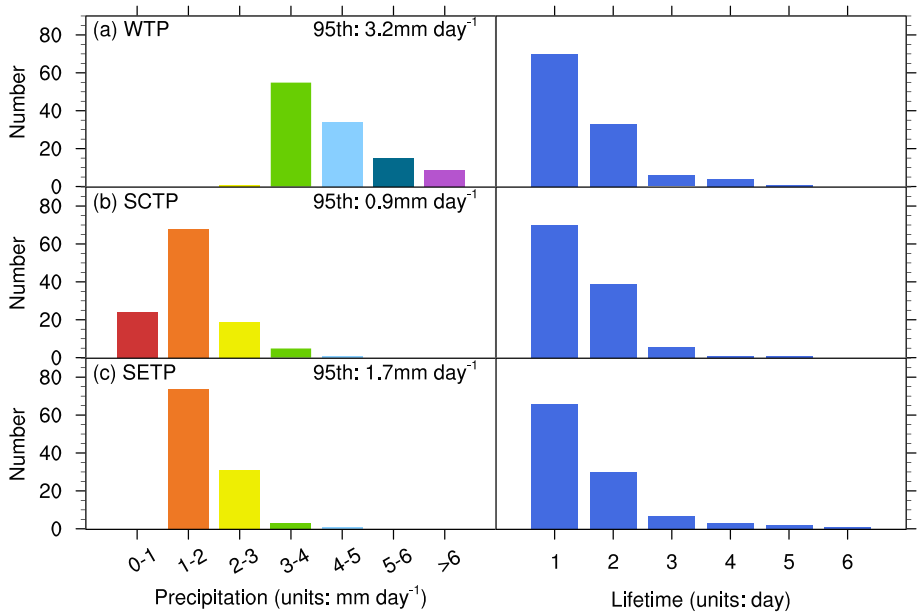

Figure 2. Frequency distributions of the precipitation intensities (left column; units: mm day^{-1}) and lifetimes (right column; units: days) of intense precipitation events derived from ERA-Interim over the (a) WTP, (b) SCTP, and (c) SETP during DJF 1979–2016. Numbers at the top right corners of left column of (a–c) represent the 95th percentiles of the daily precipitation over these three regions.

as potential moisture sources. Conversely, the geographical positions with moisture decreases along the trajectory for the same air parcel can be regarded as moisture sinks. In particular, the algorithm for estimating precipitation at each target location can be referred to Method S1 in the supporting information. Sodemann et al. (2008) further developed this approach by considering the following two aspects. First, precipitation that occurs en route may decrease the contribution of earlier moisture sources to precipitation over the target region. Second, only moisture sources within the boundary layer should be considered as evaporative moisture sources from the underlying surface. Here we adopt the above two amendments made by Sodemann et al. (2008) when using the algorithm originally developed by Stohl and James (2004).

3. Basic Characteristics of Wintertime Intense Precipitation Events

Frequency distributions of precipitation intensities for intense precipitation events in the three subregions are shown in the left column of Figure 2. The subregions listed in descending order of precipitation intensity during intense events are WTP, SETP, and SCTP, consistent with differences in the thresholds used to define the intense precipitation days in each subregion (significantly different at the 99% confidence level). In the WTP, about 91.2% of intense events have intensities ranging from 3 to 6 mm day^{-1} (Figure 2a). In comparison, intensity ranges for the majority of the intense events over the SCTP and SETP are 0 to 3 mm day^{-1} and 1 to 4 mm day^{-1}, respectively (Figures 2b and 2c). Frequency distributions of the lifetimes of intense events are similar (not significantly different at the 90% confidence level) among the three subregions (right column of Figure 2). Specifically, intense events having lifetimes of 1 day account for 61.4%, 59.8%, and 60.6% of total intense events over WTP, SCTP, and SETP, respectively, while those having lifetimes of 2 days account for 28.9%, 33.3%, and 27.5%, respectively. Few events have lifetimes exceeding 3 days.

Figures 3a–3c show the composite mean horizontal distributions of ERA-Interim precipitation over the three subregions during their respective intense events. Similar to the wintertime climatological mean, the precipitation maxima for all three subregions are concentrated along their southern slopes. This characteristic horizontal distribution of the intense precipitation events is further confirmed by using APHRODITE (Figures 3d–3f), TRMM (Figures 3g–3i), and GPCP (Figures 3j–3l) in place of ERA-Interim. As most of the wintertime intense precipitation over each subregion falls as snow (snow-to-precipitation ratios exceed 94%; see Figure S1 in supporting information), we refer to these three subregions of the TP as the snowy subregions of the TP.

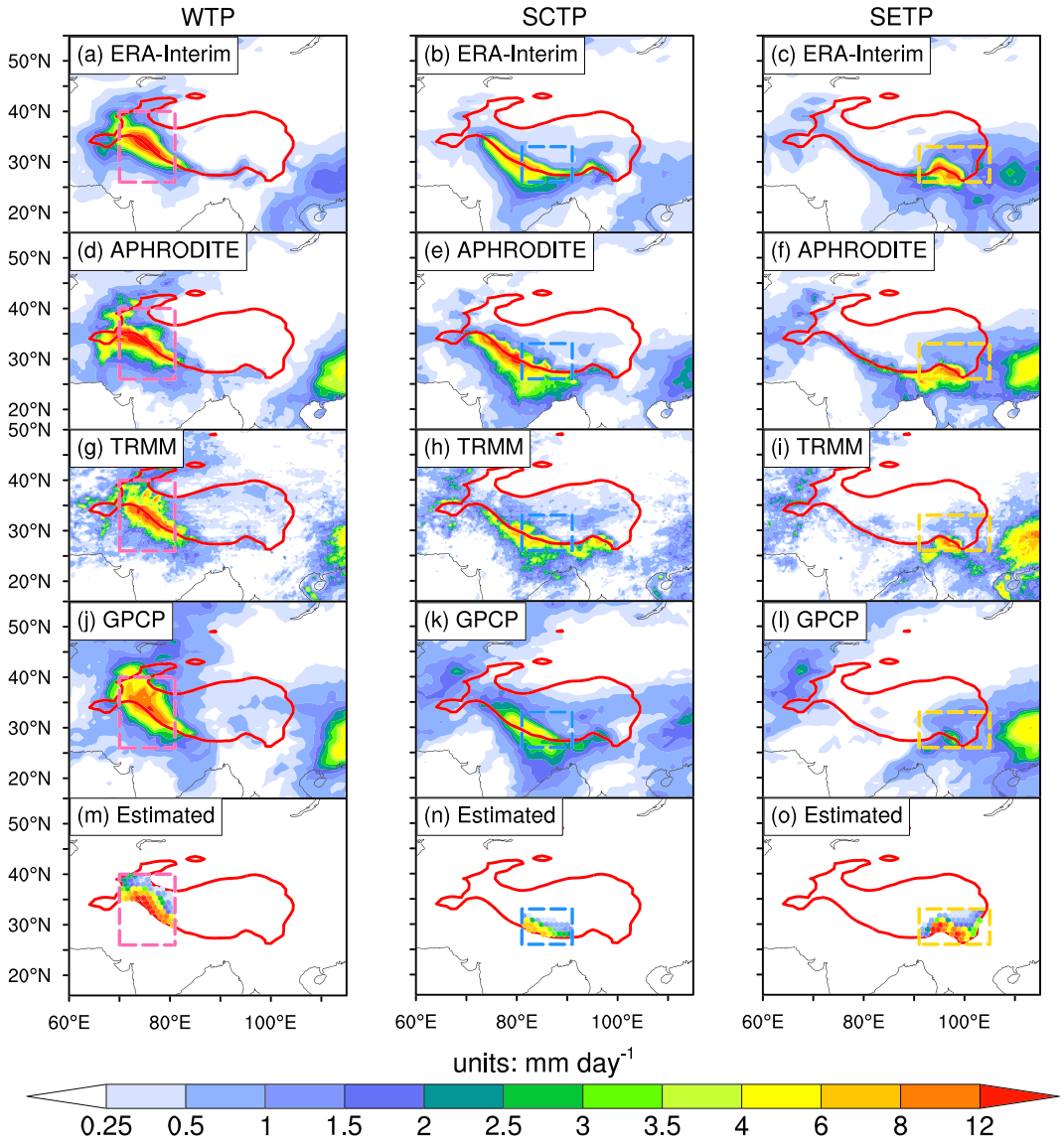

Figure 3. Horizontal distributions of average precipitation (units: mm day^{-1}) during wintertime intense precipitation events over the WTP (left), SCTP (middle), and SETP (right) based on (a–c) ERA-Interim (DJF 1979–2016), (d–f) APHRODITE (DJF 1979–2006), (g–i) TRMM (DJF 1998–2016), (j–l) GPCP (DJF 1996–2016), and (m–o) Lagrangian estimated precipitation (DJF 1979–2016). Regions bounded by solid red lines have surface altitudes higher than 2,500 m. The WTP, SCTP, and SETP are defined as the areas with surface altitudes exceeding 2,500 m within the pink, blue, and yellow dashed boxes, respectively.

Figures 3m–3o display the composite mean horizontal distribution of estimated precipitation based on the Lagrangian approach for each subregion over the TP during their respective intense precipitation events. Similar to the ERA-Interim precipitation, the estimated precipitation using the Lagrangian approach is also maximum along the southern slope of each subregion. Area-averaged precipitation values based on Lagrangian estimates (4.6 mm day^{-1} for WTP, 1.8 mm day^{-1} for SCTP, and 3.1 mm day^{-1} for SETP) are close to those based on ERA-Interim precipitation data (4.3 mm day^{-1} for WTP, 1.6 mm day^{-1} for SCTP, and 2.4 mm day^{-1} for SETP), but with slight overestimates. This overestimation issue has also been reported by previous studies (James et al., 2004; Stohl & James, 2004; Sodemann et al., 2008; Wernli & Davies, 1997) and has been attributed to two possible reasons. First, precipitation from an air parcel at the target locations of a Lagrangian trajectory is improperly overestimated in our approach as the moisture decrease of the air parcel over a 6h interval. Second, many complex microphysical processes are neglected when estimating precipitation using the Lagrangian approach. These processes are replaced by the relatively crude criteria

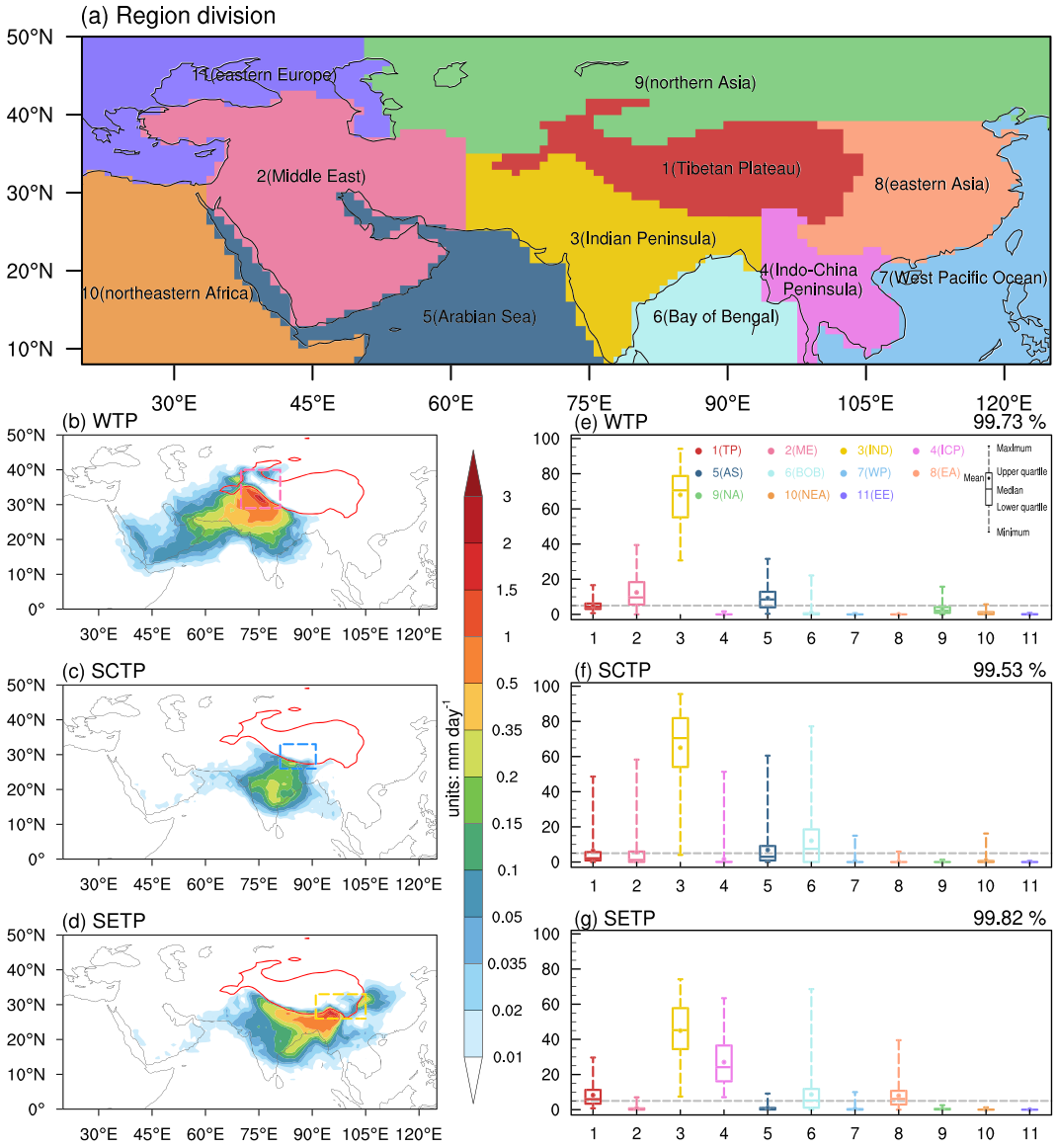

Figure 4. (a) Definition of the 11 sectors used for diagnosing and attributing moisture sources. Horizontal distributions of average attributed evaporative moisture sources (units: mm day^{-1}) for wintertime intense precipitation events over the (b) WTP, (c) SCTP, and (d) SETP, respectively. Regions bounded by solid red lines have surface altitudes higher than 2,500 m. The WTP, SCTP, and SETP are defined as the areas with surface altitudes exceeding 2,500 m within the dashed box in the corresponding panel. (e–g) Box-and-whisker diagrams summarizing relative evaporative moisture contribution ratios (units: %) from the 11 named sectors to the identified intense precipitation events over the WTP, SCTP, and SETP. In each box-whisker plot, the horizontal line across the box and the lower and upper boundaries represent the median and lower and upper quartiles, respectively, while the dot and lower and upper whiskers denote the mean, minimum, and maximum, respectively. Numbers at the top right of (e)–(g) represent the sum of contributions from the 11 named sectors.

of a moisture decrease along the Lagrangian trajectory and relative humidity ≥80%. Huang et al. (2018) pointed out that the estimated precipitation intensity is sensitive to the relative humidity threshold defined for the occurrence of precipitation. However, despite this slight overestimation of precipitation intensity, the Lagrangian approach effectively reproduces the spatial patterns and relative intensities of precipitation over these three subregions of the TP. Thus, it is reasonable to adopt the Lagrangian approach for inferring the geographical distributions of evaporative moisture sources for wintertime intense precipitation events over the WTP, SCTP, and SETP domains.

4. Evaporative Moisture Sources for the Three Subregions Over the TP

Figures 4b–4d illustrate the composite mean horizontal distribution of evaporative moisture sources estimated for intense precipitation events over each of the three subregions.

For the WTP, evaporative moisture sources exceeding 0.05 mm day^{-1} have a widespread distribution that extends southwestward from the northern part of the Indian Peninsula to the Red Sea. Moisture contributions from the northern and central Indian Peninsula, the eastern Middle East, and the northern Arabian Sea all exceed 0.2 mm day^{-1}. The moisture contribution peaks over the southern slope of the WTP (with surface altitudes <2,500 m) with a magnitude of 1 mm day^{-1}.

For the SCTP, evaporative moisture sources exceeding 0.05 mm day^{-1} are confined to the central and northern parts of the Indian Peninsula, much narrower than those for the WTP. The moisture source distribution has two localized maxima with magnitudes exceeding 0.2 mm day^{-1}. One maximum is located over the central Indian Peninsula, while the other is located over the southern slope of the SCTP (with surface altitudes <2,500 m).

For the SETP, source regions with moisture contributions exceeding 0.05 mm day^{-1} are again widespread. The specific source regions include the majority of the Indian Peninsula and the Sichuan basin east of the TP. The maximum moisture contributions, with a magnitude of 1 mm day^{-1}, are located along the southern slope of the SETP (with surface altitudes <2,500 m).

To compare the relative quantitative contributions of moisture from different source regions to wintertime intense precipitation events over the three subregions, we divide the TP and its surrounding areas into 11 separate sectors (Figure 4a). These 11 sectors include (1) the TP, (2) the Middle East, (3) the Indian Peninsula, (4) the Indo-China Peninsula, (5) the Arabian Sea, (6) the Bay of Bengal, (7) the West Pacific Ocean, (8) eastern Asia, (9) northern Asia, (10) northeastern Africa, and (11) eastern Europe. The contribution ratio for a specific sector (Figures 4e–4g) is estimated as the ratio between the area integral of moisture contributions from this sector and that of moisture contributions from the whole sphere. Note that the 11 sectors shown in Figure 4a contribute more than 99.5% of the moisture for intense precipitation over the three subregions. Thus, all key moisture source regions for intense precipitation over these three subregions of the TP are included in the analysis.

For intense precipitation over the WTP, sectors with mean relative contributions ≥ 5% include the Indian Peninsula (contributing 68.0%), the Middle East (12.5%), the Arabian Sea (9.2%), and the TP (5.0%) (Figure 4e). Thus, the Indian Peninsula plays a dominant role in supplying moisture for intense precipitation over the WTP. However, moisture contributions from the Indian Peninsula vary substantially from case to case, with relative contributions ranging from 30.7% to 94.2%. We further divide the moisture contribution into three parts: local contributions (from the WTP itself), contributions from terrestrial regions outside the WTP, and contributions from oceanic regions. The relative contributions from these three domains are 3.9% (local), 85.7% (terrestrial), and 10.4% (oceanic), respectively. The key oceanic source region is the Arabian Sea, with relative contributions ranging from 0.3% to 31.6%. Therefore, the terrestrial areas provide most of the moisture for intense precipitation events over the WTP.

For intense precipitation over the SCTP, the five moisture source regions with mean relative contributions ≥5% include the Indian Peninsula (contributing 65.0%), the Bay of Bengal (12.1%), the Arabian Sea (6.9%), the TP (6.5%), and the Middle East (5.6%) (Figure 4f). The relative contributions from the Indian Peninsula, the Bay of Bengal, and the Arabian Sea vary substantially across events. Specifically, the maximum relative contributions from these three regions are 95.5%, 77.2%, and 60.5%, respectively, while the minimum relative contributions are 4.0%, 0.0%, and 0.0%, respectively. The relative contributions of local (from the SCTP), other terrestrial, and oceanic sources are 5.5%, 74.8%, and 19.8%, respectively. Thus, oceanic sources play a more important role in supporting intense precipitation over the SCTP (contributing 19.8%) than over the WTP (10.4%). However, terrestrial sources, and especially the Indian Peninsula, still play the leading role in supplying moisture for intense precipitation over the SCTP.

For intense precipitation over the SETP, the five moisture source regions with mean relative contributions ≥5% include the Indian Peninsula (contributing 45.0%), the Indo-China Peninsula (27.0%), the Bay of Bengal (8.6%), the TP (8.3%), and East Asia (8.0%) (Figure 4g). Although the Indian Peninsula still plays a leading role in moisture supply for the intense precipitation over the SETP, its mean relative contribution is much

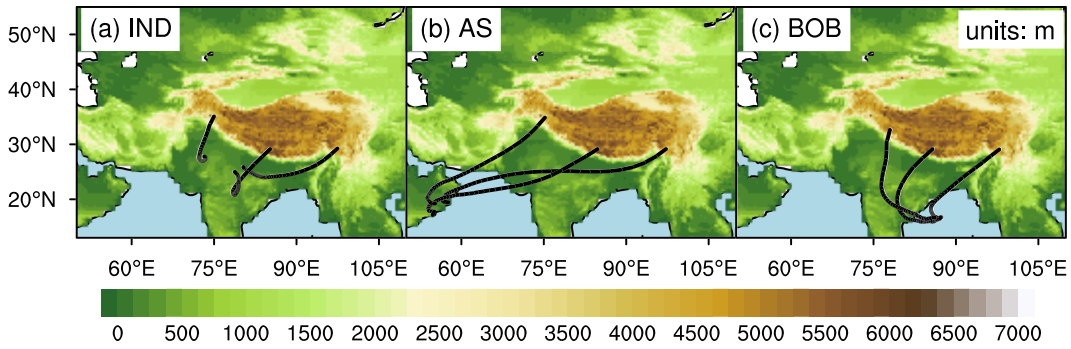

Figure 5. Characteristic trajectories (black curve) of moisture transport from (a) the Indian Peninsula, (b) the Arabian Sea, and (c) the Bay of Bengal to the WTP, SCTP, and SETP preceding wintertime intense precipitation events. Shading represents surface altitude (units: m).

lower than those computed for the WTP and SCTP. In addition, the mean relative contribution from the Indo-China Peninsula to the SETP is much larger than that to the WTP and SCTP combined. The relative contributions from the Indian Peninsula, the Indo-China Peninsula, the Bay of Bengal, and East Asia vary greatly from case-to-case. The maximum relative contributions from these four regions are 74.2%, 63.4%, 68.6%, and 39.5%, while the minimum relative contributions are 7.5%, 7.1%, 0.0%, and 0.0%. The relative contributions of local (from the SETP), other terrestrial, and oceanic sources are 5.6%, 84.1%, and 10.3%, respectively.

Therefore, most (≥70%) of the moisture for intense precipitation over each of the three subregions of the TP comes from terrestrial areas. In particular, the Indian Peninsula plays a leading role in providing moisture for all three subregions. For each subregion, a localized maximum in the moisture contribution is evident over the southern slope of the TP with lower surface altitudes. Thus, we speculate that some lifting processes (such as orographic lifting) play crucial roles in delivering air parcels with abundant moisture to the target subregions within the TP during intense precipitation events.

5. Characteristic Trajectories for the Moisture Transports From the Key Moisture Source Regions to the Three Subregions

As demonstrated in Section 4, the key terrestrial moisture source region for wintertime intense precipitation events in all three subregions of the TP is the Indian Peninsula, while the key oceanic moisture source regions are the Arabian Sea and the Bay of Bengal. This section describes the characteristic trajectories for moisture transports from these three key moisture source regions to the three subregions of the TP.

Our method for estimating the characteristic trajectory from an arbitrary source region (Region S) to a specific target region (Region T) consists of the following two steps.

Step 1: Identify those trajectories along which there is at least one point within Region S with moisture contribution ≥0.02 mm day^{-1} to the precipitation over Region T. The earliest point within Region S exceeding this threshold contribution between −240 hr and −6 hr is viewed as the starting position of the moisture transport trajectory linking Region S to Region T. All points along the trajectory before this starting position are discarded.

Step 2: Calculate the geographical position of the characteristic trajectory linking Region S to Region T at a specific relative time step (from −240 hr to 0 hr with an interval of 6 hr) as the mean of all identified trajectory points at the same relative time step. Any points along the trajectories that are removed in Step 1 are not considered in Step 2.

Figure 5 shows the characteristic trajectories from the three key source regions, including the Indian Peninsula, the Arabian Sea, and the Bay of Bengal, to the three target regions, including the WTP, SCTP, and SETP. Due to long transport pathways from the Arabian Sea and Bay of Bengal to the three subregions, much of the moisture evaporated from these oceanic sources is lost en route. Moreover, characteristic trajectories can traverse more than one region with relatively large moisture contributions. Indian Peninsula contributions along Arabian Sea trajectories and Bay of Bengal trajectories to the WTP respectively account for 29.1% and 3.5% of the moisture contributions integrated over the entire globe (Figure S2 in supporting

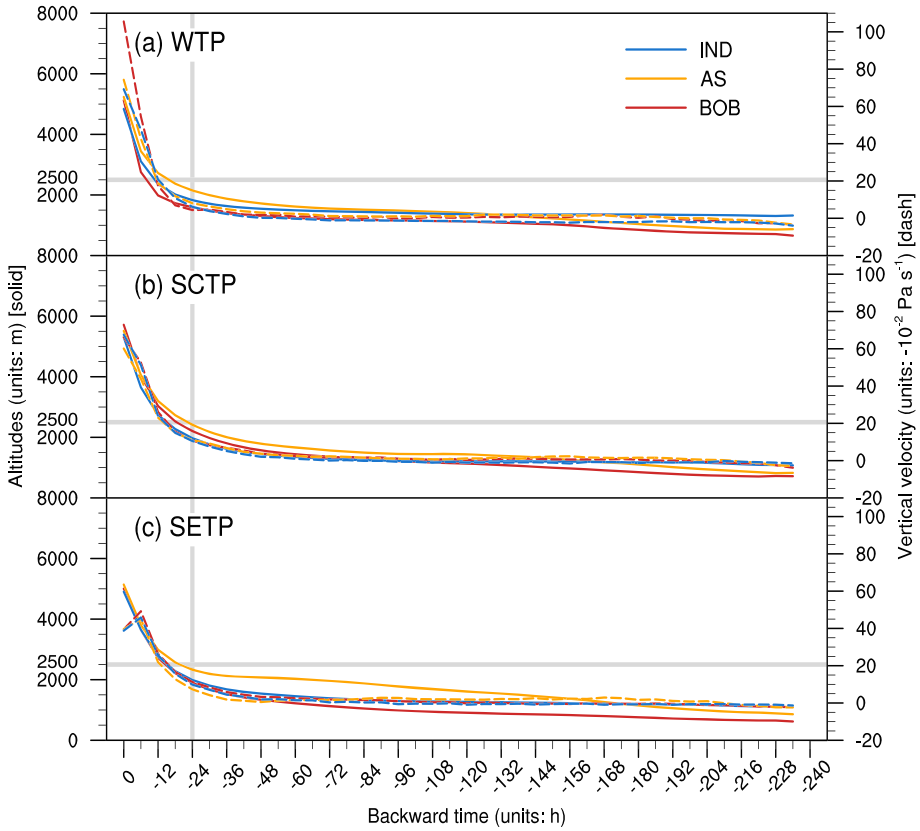

Figure 6. Evolution of the altitudes (units: m; dashed line; left ordinate) and vertical velocity (units: 10^{-2} Pa s^{-1}; solid line; right ordinate) backward in time (from −240 hr to 0 hr) along characteristic trajectories. The characteristic trajectories represent moisture transport from the Indian Peninsula (blue), Arabian Sea (orange), and Bay of Bengal (red) to the (a) WTP, (b) SCTP, and (c) SETP.

information). The sum of these two contributions (contribution ratio: 32.6%) is close to half of the contributions from the Indian Peninsula to the WTP (relative contribution: 68.0%). The contribution ratio of moisture evaporated from the Indian Peninsula to the SCTP along the above two oceanic trajectories is 44.4%, while that to the SETP is 24.7%. These two ratios are more than half of the relative contributions from the Indian Peninsula to the SCTP (65.0%) and SETP (45.0%). Therefore, a large part of the moisture evaporated from the Indian Peninsula is transported along trajectories that also pass over the Arabian Sea or Bay of Bengal.

For target regions with high surface altitudes, it is more critical to identify the vertical variations along these characteristic trajectories than the horizontal variations. Figure 6 shows evolutions of altitude and vertical velocity along the nine characteristic trajectories. All nine characteristic trajectories are characterized by mean altitudes less than 2,500 m between −240 hr and −24 hr, indicating that the key moisture transport pathways are mainly modulated by the lower-tropospheric circulation. In the last 24 hr, the air parcels along these characteristic trajectories ascend suddenly from 2,500 m to 5,000 m. At the same time, the vertical velocities of these air parcels rapidly increase from around −0.01 Pa s^{-1} (slightly upward) between −240 hr and −24 hr to around −0.2 Pa s^{-1} (sharply upward) between −24 hr to 0 hr. Therefore, we suggest that orographic lifting due to the presence of steep topography plays an important role in supplying moist air parcels to the three high-altitude target regions. Uplift of air parcels that occurs mainly in the 24 hr preceding the event can be easily understood. Earlier uplift of air parcels could result in earlier precipitation along their northward transport pathways, meaning that these air parcels are more dehydrated when they reach the target regions.

The characteristic time scale for moisture transport from each source region to the corresponding target region provides a useful indicator for the time periods over which to evaluate the evolution of favorable circulation patterns and associated thermodynamic variables. Figure 7 shows characteristic time scales for moisture transport from the same three source regions to the three target regions. Here the characteristic

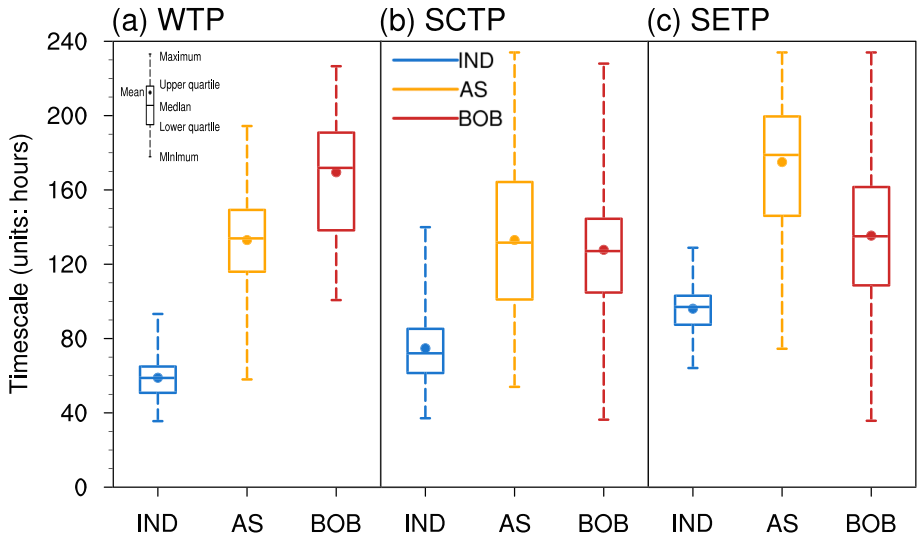

Figure 7. Box-and-whisker diagrams summarizing the distributions of characteristic transport time scales for moisture transport from the Indian Peninsula (blue), Arabian Sea (orange), and Bay of Bengal (red) to the (a) WTP, (b) SCTP, and (c) SETP preceding wintertime intense precipitation events.

time scale for moisture transport linking moisture originating from Region S to the target Region T is calculated as the weighted average of time elapsed between all moisture contributions ≥0.02 mm day^{-1} in source regions and the corresponding precipitation point over Region T. The mean characteristic time scales for moisture from the Indian Peninsula to reach the WTP, SCTP, and SETP are 2.5, 3.1, and 4.0 days, respectively, much shorter than the characteristic transport timescales from the Arabian Sea and the Bay of Bengal. The mean characteristic time scales for moisture transport from the Arabian Sea to the WTP, SCTP, and SETP are 5.5, 5.4, and 7.3 days, respectively, while those from the Bay of Bengal are 7.1, 5.3, and 5.6 days. Note that characteristic time scales for moisture transport from the Arabian Sea and the Bay of Bengal to the three subregions are highly variable. The minimum time scales for moisture transport from the Arabian Sea to the WTP, SCTP, and SETP are 2.4, 2.3, and 3.1 days, respectively, while the maximum timescales are 8.1, 9.8, and 9.8 days. Time scales for moisture transport from the Bay of Bengal to the SCTP and SETP range from around 1.5 days to 9.6 days, while those for transport from the Bay of Bengal to the WTP range from 4.2 to 9.4 days.

6. Favorable Circulation Patterns for Moisture Transport

In this study, the favorable circulation pattern (FCP) linking moisture from a specific source region to the target region within the TP is estimated using the formula:

$$\mathrm{FCP} = \frac{1}{N}\sum_{i=1}^{N}\sum_{m=-10}^{L_i-1} \mathrm{CP}_i^m w_i^m, \tag{1}$$

where N is the total number of intense precipitation events over the target region with moisture contributions from the source region ≥70th percentile, and L_i is the duration of the ith intense precipitation event, m is the index of the day relative to the onset of the ith intense precipitation event, CP_i^m is the circulation pattern at 850 hPa on Day m of the ith event, and w_i^m is the corresponding weight. Considering that the circulation pattern on Day m can transport moisture contribution from Day −10 to Day m, the weight coefficient w_i^m is calculated as:

$$w_i^m = \frac{\sum_{j=-10}^{m} Q_i^j}{\sum_{m=-10}^{L_i-1}\sum_{j=-10}^{m} Q_i^j}, \tag{2}$$

where Q_i^j is the moisture contribution from the source region on Day j of the ith intense event. According to this formula, the weight for the circulation pattern on Day m is assigned to match the sum of moisture contributions from Day −10 to Day m.

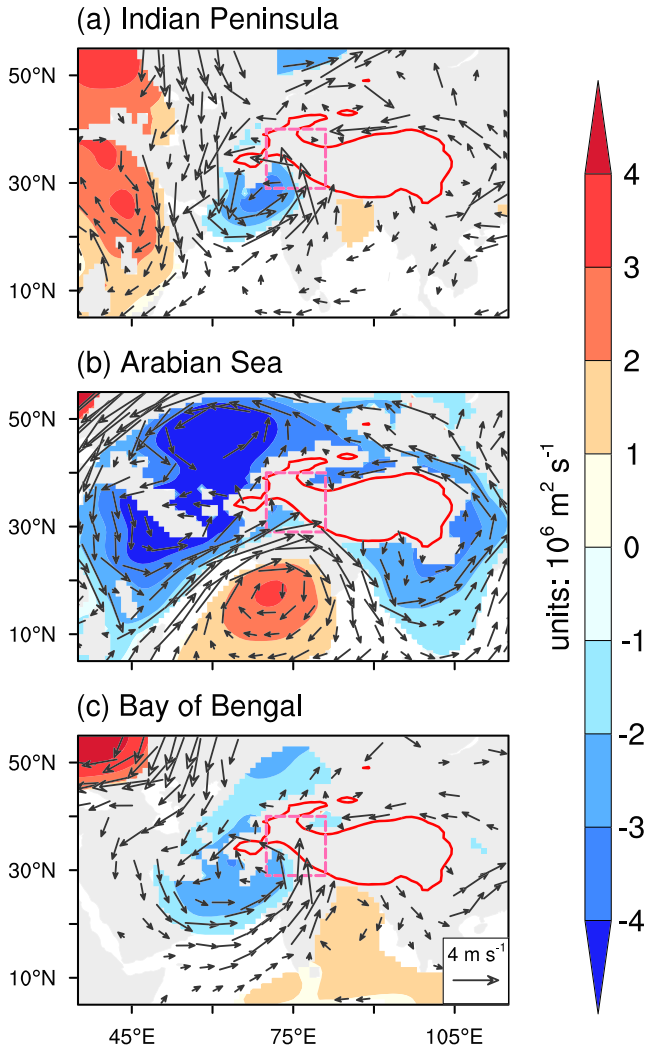

Figure 8. Composite stream function anomalies (shading; units: 10^6 m^2 s^{-1}) and horizontal wind anomalies (vectors; units: m s^{-1}) at 850 hPa for moisture transport to wintertime intense precipitation events over the WTP with large (≥70th percentile) moisture contributions from the (a) Indian Peninsula, (b) Arabian Sea, and (c) Bay of Bengal. Shading and vectors are only shown when composite anomalies meet the 95% confidence level based on two-tailed Student's *t* tests. Note that vectors are plotted if wind anomalies are significant in at least one direction (zonal or meridional). Regions bounded by solid red lines have surface altitudes higher than 2,500 m. The WTP is defined as the area with surface altitudes exceeding 2,500 m within the pink dashed box.

We focus on the 850-hPa isobaric surface in evaluating the favorable circulation patterns mainly because moisture is primarily transported in the lower troposphere between the key moisture source regions and the three subregions of the TP (see Section 5).

6.1. Favorable Circulation Patterns for the Moisture Transport to the WTP

The favorable circulation patterns for moisture transport from the three key source regions to the WTP are all characterized by a significant cyclonic anomaly anchored near the northwestern Indian Peninsula (southwest of the WTP; Figures 8a–8c). In the favorable circulation pattern for moisture transport from the Indian Peninsula to the WTP, the cyclonic anomaly has a peak stream function magnitude exceeding 3 × 10^6 m^2 s^{-1} and is confined to the north of 25°N (Figure 8a). Supported by a weak anticyclonic anomaly over the northeastern Indian Peninsula, southerly wind anomalies downstream of the cyclonic anomaly cover the majority of the Indian Peninsula. These southerly anomalies effectively prompt moisture transport from the Indian Peninsula to the WTP. In the favorable circulation pattern for moisture transport from the Bay of Bengal, the cyclonic anomaly expands southeastward over the central Arabian Sea and the anticyclonic anomaly expands southward over the Bay of Bengal (Figure 8c). These expansions mean that southerly wind anomalies downstream of the cyclonic anomaly reach over the Bay of Bengal, intensifying the moisture transport from this region to the WTP. Despite these differences in extent, the favorable circulation patterns for moisture transport from the Indian Peninsula and moisture transport from the Bay of Bengal are similar. This similarity can be partially explained by the fact that many of the intense precipitation events used to identify favorable circulation patterns for moisture transport from these two source regions are the same.

In the favorable circulation pattern for moisture transport from the Arabian Sea, a cyclonic anomaly with a peak stream function magnitude exceeding 4 × 10^6 m^2 s^{-1} expands further southwestward to cover the entire area west of the WTP (Figure 8b). Powerful southwesterly wind anomalies downstream of the cyclonic anomaly are conducive to moisture transport from the northwestern Arabian Sea to the WTP. It is worth noting the presence of a significant anticyclonic anomaly to the south of the cyclonic anomaly. Downstream of this anticyclonic anomaly, strong northerly wind anomalies inhibit moisture transport from the Indian Peninsula and the Bay of Bengal to the WTP.

6.2. Favorable Circulation Patterns for the Moisture Transport to the SCTP

The favorable circulation patterns for moisture transport from the three key source regions to the SCTP are all characterized by a significant cyclonic anomaly over the northern Indian Peninsula (southwest of the SCTP; Figures 9a–9c). In the favorable circulation pattern for moisture transport from the Indian Peninsula, the cyclonic anomaly has a peak stream function magnitude exceeding 2×10^6 m^2 s^{-1} and is confined within 60°E to 75°E (Figure 9a). Southwesterly wind anomalies downstream of this cyclonic anomaly cover the majority of the Indian Peninsula, favoring moisture transport from the Indian Peninsula to the SCTP. In the favorable circulation pattern for moisture transport from the Arabian Sea, the cyclonic anomaly expands eastward over the northeastern Indian Peninsula and displays an elongated east-west orientation (Figure 9b). The peak magnitude of the cyclonic anomaly exceeds 4 ×10^6 m^2 s^{-1}, much larger than that under the favorable circulation pattern for moisture transport from the Indian Peninsula (Figure 9a). South of this intense cyclonic anomaly, powerful westerly wind anomalies over the Arabian Sea favor moisture transport from the Arabian Sea to the

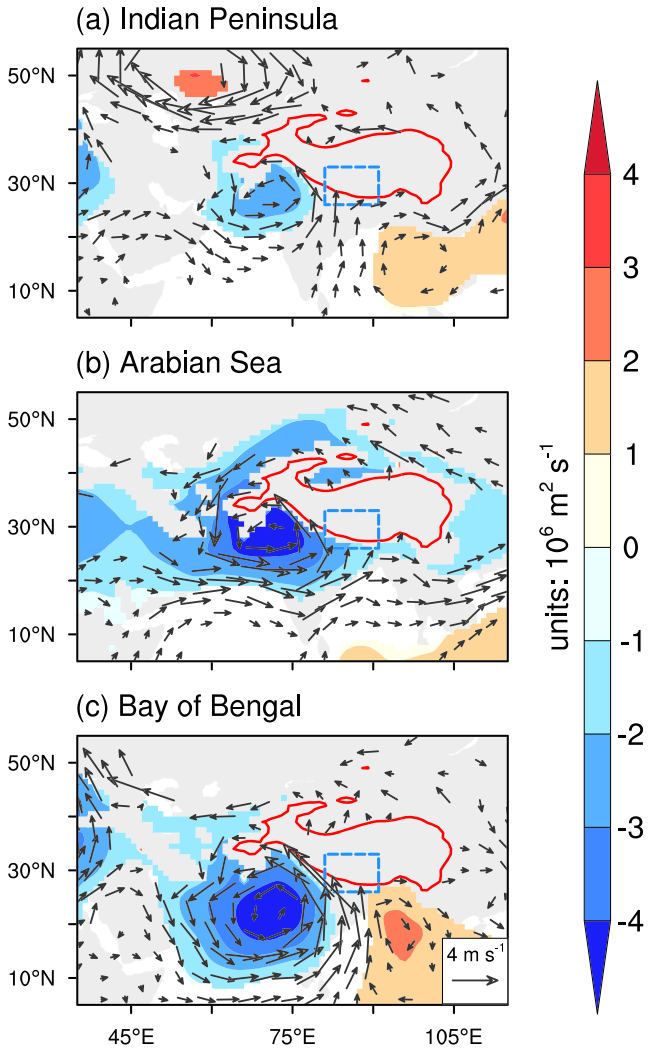

Figure 9. Composite stream function anomalies (shading; units: 10^6 m^2 s^{-1}) and horizontal wind anomalies (vectors; units: m s^{-1}) at 850 hPa for moisture transport to wintertime intense precipitation events over the SCTP with large (≥70th percentile) moisture contributions from the (a) Indian Peninsula, (b) Arabian Sea, and (c) Bay of Bengal. Shading and vectors are only shown when composite anomalies meet the 95% confidence level based on two-tailed Student's *t* tests. Note that vectors are plotted if wind anomalies are significant in at least one direction (zonal or meridional). Regions bounded by solid red lines have surface altitudes higher than 2,500 m. The SCTP is defined as the area with surface altitudes exceeding 2,500 m within the blue dashed box.

atmosphere above the Indian Peninsula (Figure 9b). The enhanced southwesterly wind anomalies downstream of the cyclonic anomaly then deliver the moisture to the SCTP (Figure 9b). In the favorable circulation pattern for moisture transport from the Bay of Bengal, the cyclonic anomaly is shifted further south, covering nearly the whole Arabian Sea and Indian Peninsula (Figure 9c). Supported by an anticyclonic anomaly over the Bay of Bengal, this southward expansion induces southerly wind anomalies over the western Bay of Bengal, to the east of the cyclonic anomaly. This situation effectively promotes moisture transport from the Bay of Bengal to the SCTP.

6.3. Favorable Circulation Patterns for the Moisture Transport to the SETP

The favorable circulation pattern for moisture transport from the Indian Peninsula to the SETP is characterized by a significant anticyclonic anomaly over the tropical Arabian Sea and Bay of Bengal (Figure 10a). As a consequence, westerly wind anomalies prevail over most of the Indian Peninsula, favoring the eastward transport of moisture from the Indian Peninsula to the southern part of the SETP. The favorable circulation pattern for moisture transport from the Arabian Sea features a significant cyclonic anomaly over the northern Indian Peninsula (southwest of the SETP) and anomalous anticyclonic centers over the tropical Arabian Sea and Bay of Bengal (Figure 10b). Southwesterly wind anomalies downstream of the cyclonic anomaly favor moisture transport from the Arabian Sea to the SETP. Note that the anticyclonic anomaly over the tropical Bay of Bengal is remarkably stronger under this situation, intensifying eastward moisture transport from the Arabian Sea. Owing to the distance between the Arabian Sea and the SETP, the mean relative contribution of the Arabian Sea to intense precipitation over the SETP under the favorable situation is still only 2.9%. In the favorable circulation pattern for moisture transport from the Bay of Bengal, the cyclonic anomaly expands southeastward over the western Bay of Bengal (Figure 10c). Under this situation, nearly the entire Bay of Bengal is covered by strong southerly wind anomalies, supporting a mean relative contribution of 21.0%.

7. Discussion

In this section, we discuss in more detail the roles of two specific features of the large-scale circulation: the warm conveyor belt and the Rossby wave train. These circulations contribute in important ways to the formation of wintertime intense precipitation events over the three subregions of the TP.

7.1. Warm Conveyor Belt

As mentioned in Section 6, southerly winds downstream of the lower-tropospheric cyclonic anomaly are crucial for moisture transport from the south to the Himalayan foothills. It is therefore necessary to analyze the thermodynamic conditions in the lower troposphere preceding intense precipitation events. Figures S3–S8 (in supporting information) show the composite evolutions of temperature and specific humidity anomalies on the 850-hPa isobaric surface from Day −8 to Day 0 for wintertime intense precipitation events over the WTP, SCTP, and SETP, respectively. Intense precipitation events over each of the three subregions are associated with significant warm temperature anomalies to the southwest of the corresponding subregion (Figures S3–S5). These warm temperature anomalies last from Day −6 to Day 0 for events over the WTP and SETP, but from Day −2 to Day 0 for events over the SCTP. The amplitudes of these warm temperature anomalies all exceed 0.5 K. Moreover, large parts of these significant warm temperature anomalies are

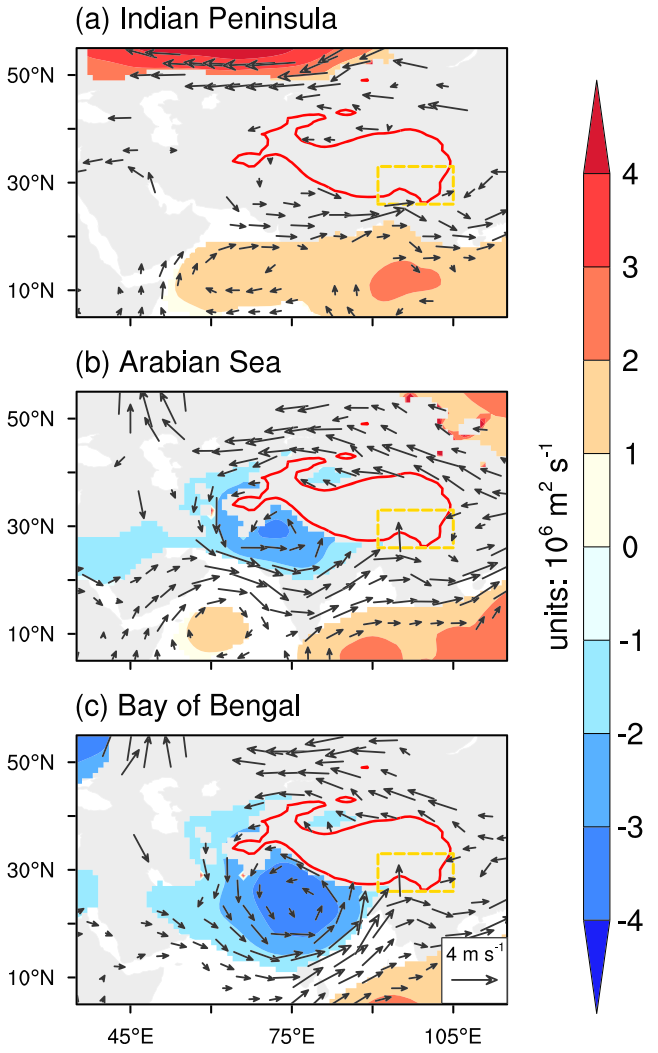

Figure 10. Composite stream function anomalies (shading; units: 10^6 m^2 s^{-1}) and horizontal wind anomalies (vectors; units: m s^{-1}) at 850 hPa for moisture transport to wintertime intense precipitation events over the SETP with large (≥70th percentile) moisture contributions from the (a) Indian Peninsula, (b) Arabian Sea, and (c) Bay of Bengal. Shading and vectors are only shown when composite anomalies meet the 95% confidence level based on two-tailed Student's *t* tests. Note that vectors are plotted if wind anomalies are significant in at least one direction (zonal or meridional). Regions bounded by solid red lines have surface altitudes higher than 2,500 m. The SETP is defined as the area with surface altitudes exceeding 2,500 m within the yellow dashed box.

geographically coincident with significant positive anomalies in specific humidity (Figures S6–S8). From Day −2 to Day 0, the warm and humid anomalies are approximately collocated with regions identified as contributing relatively large amounts of moisture to intense precipitation events over the corresponding subregion (Figures 4b–4d). As mentioned in Section 5, strong updrafts are observed southwest of each subregion leading up to intense precipitation events. Therefore, the regions with warm temperature anomalies and positive specific humidity anomalies may be regarded as a warm conveyor belt, which is defined as a coherent warm, moist, and ascending flow (Madonna et al., 2014). As documented by Madonna et al. (2014) and Pfahl et al. (2014), the presence of a warm conveyor belt favors the formation of extreme precipitation.

7.2. Rossby Wave Train

Huang et al. (2018) showed that the Rossby wave train in the upper troposphere plays a crucial role in the development of extreme precipitation events (defined based on the 99th percentile) over the SETP region. Figure S9 shows the composite evolution of geopotential height anomalies on the 300-hPa isobaric surface from Day −12 to Day 0 for intense precipitation events that occurred over the WTP. A significant anticyclonic anomaly forms over the eastern Atlantic Ocean about 12 days before the onset of intense precipitation events over the WTP (Figure S9a). This anticyclonic anomaly persists until Day −1 (Figures S9a–S9h). The anticyclonic anomaly is located over western Europe on Day −1, close to its position on Day −12. Considering its remarkable persistence and quasi-stationarity, this anticyclonic anomaly can be viewed as a blocking high. The presence of a blocking high over western Europe plays an essential role in both triggering and strengthening the downstream cyclonic anomalies. By day −4, a Rossby-like wave train consisting of four action centers has formed, comprising the anticyclonic anomaly over western Europe, a cyclonic anomaly downstream of this anticyclonic anomaly, a second anticyclonic anomaly over the Middle East, and a second cyclonic anomaly over southern Asia. By Day 0, the eastern edge of the cyclonic anomaly downstream of the European anticyclonic anomaly has migrated over the WTP, where it promotes the development of strong updrafts, large-scale moisture convergence, and intense precipitation. The development of this cyclonic anomaly is further supported by the Rossby wave train along the subtropical jet stream between Day −4 and Day −2.

For the SCTP, the favorable circulation pattern leading to intense precipitation is characterized by a Rossby wave train embedded in the subtropical jet (Figure S10f). This zonally oriented Rossby wave train includes two anticyclonic anomalies over northwestern Africa and the Middle East and two cyclonic anomalies over northern Africa and the WTP. The movement of the easternmost cyclonic anomaly toward the SCTP and triggers the conditions required for intense precipitation to occur there. The favorable circulation pattern for the intense precipitation events over the SETP is also characterized by a Rossby wave train embedded in the subtropical jet (Figure S11g), although this Rossby wave train has more centers of action than that for the SCTP. Intense precipitation over the SETP is associated with the eastward migration of a cyclonic anomaly from the WTP toward the SETP (Figures S11g–S11i).

We further analyze the composite evolutions of temperature anomalies on the 500-hPa isobaric surface associated with the development of intense precipitation events over each of the three subregions (Figures S12–S14). Note that the 500-hPa isobaric surface is located close to the surface in all three subregions. Before the onset of intense precipitation in each subregion, significant warm temperature anomalies propagate into that subregion from the west. The presence of these warm temperature anomalies is closely related to cold advection downstream of the anticyclonic anomaly (i.e., west of the cyclonic anomaly that produces

intense precipitation over the target region). Because the anticyclonic anomalies for both the SCTP and SETP region are effectively embedded in the subtropical jet stream, the intrusion of cold air from higher latitudes is very weak. By contrast, the presence of the blocking high over western Europe preceding intense precipitation events over the WTP favors strong cold air intrusions from higher latitudes into the WTP region. As a consequence, significant cold temperature anomalies at 500 hPa cover essentially the entire latitude band west of the WTP from south of 30°N to around 60°N between Day −3 and Day 0 (Figures S12b–S12e). This intrusion of cold air from the north not only enhances updrafts by lifting warm air but also helps to transform precipitable water into precipitation by lowering saturation thresholds for water vapor through much of the atmospheric column. Cold air from the extratropics thus plays an indispensable role in the formation of wintertime intense precipitation events over the WTP. It is interesting to note that Martius et al. (2013) documented similar extratropical-tropical interactions during the formation of a summertime extreme precipitation event that led to extensive flooding in Pakistan in July 2010.

8. Summary and Concluding Remarks

Wintertime intense precipitation events over the TP are frequently accompanied by severe snow disasters. In this study, a Lagrangian approach is employed to examine the evaporative moisture sources for wintertime intense precipitation events over the three snowy subregions of the TP during DJF 1979–2016. It is revealed that most of the moisture supply for wintertime intense precipitation events over the WTP, SCTP, and SETP originates from terrestrial areas outside the target region, accounting for 85.7%, 74.8%, and 84.1% of intense precipitation, respectively. In particular, the Indian Peninsula consistently plays a leading role in providing moisture for the three snowy subregions, with mean contributions of 68.0% for the WTP, 65.0% for the SCTP, and 45.0% for the SETP. Transports from oceanic areas play a lesser role on average (10.4% for WTP, 19.8% for SCTP, and 10.3% for SETP) but are major contributors in certain cases, with the Arabian Sea and the Bay of Bengal representing the two primary oceanic source regions. Evaporative moisture sources for intense precipitation over the WTP and SETP have widespread distributions. Relative contributions of the Arabian Sea to intense precipitation over the WTP and SETP are 9.2% and 1.1%, respectively, while the Bay of Bengal contributes 1.1% and 8.6%. The evaporative moisture source distribution for the SCTP is mostly confined to the Indian Peninsula. Despite this narrow moisture source distribution, the Arabian Sea (6.9%), and Bay of Bengal (12.1%) nonetheless still play important roles.

The moisture supplies from the three source regions mentioned above (the Indian Peninsula, Arabian Sea, and Bay of Bengal) to the three snowy subregions of the TP are all characterized by lower-level moisture transport from the south to the Himalayan foothills. The lower-level moisture transport pathways consistently involve southerly winds downstream of a cyclonic anomaly over the Indian Peninsula, further supported by an anticyclonic anomaly over the tropical Arabian Sea and Bay of Bengal. In particular, no matter how the cyclonic anomaly shifts, expands, or intensifies, it is always located to the southwest of the target region. As air parcels approach the target regions (mainly during the last 24 hr), ascending air parcels carry moisture from the foothills to the three high-altitude target regions. This lifting is supported by the combined effect of the orographic lifting and favorable large-scale circulation patterns.

In a companion paper, Huang et al. (2018) have examined the moisture sources for wintertime extreme precipitation events over the SETP. During winter, high-intensity precipitation events over the TP mainly occur along the southern periphery, which includes not only the SETP but also the WTP and SCTP subregions. Therefore, identifying and investigating the moisture sources for wintertime intense precipitation events over all three subregions provides a more comprehensive picture of the wintertime hydrological cycle in the vicinity of the TP. Note that Huang et al. (2018) analyzed 27 wintertime extreme precipitation events identified based on the 99th percentile of all daily precipitation records during winter. By contrast, the intense precipitation events examined in this study are identified based on the 95th percentile, yielding at least 109 wintertime intense precipitation events in each subregion. The findings of this study can thus be applied to a larger population of intense precipitation events over the TP and its south slope. We have proposed a method to determine the favorable circulation patterns linking moisture from a given source region to each target region (in this case, the three subregions). Huang et al. (2018) also discussed favorable circulation patterns for moisture transport; however, their approach was based on the composite evolution of geopotential height anomalies. The method we apply in this paper provides a fuller and more objective characterization of the favorable circulation patterns and their influences on moisture transport. Moreover, we find that the favorable

upper tropospheric circulation pattern preceding the onset of intense precipitation events over the WTP differs from those for events over the SCTP and SETP. A blocking high over western Europe plays a crucial role in the formation of the intense precipitation events over the WTP. This blocking high helps to intensify the cyclonic anomaly around the WTP and promote the intrusion of cold air from the extratropics to the WTP. The cyclonic anomaly and cold air intrusion both favor the onset of the intense precipitation events.

Regarding the moisture sources for wintertime precipitation over the TP, our results differ in some respects with those of previous studies. Previous studies have indicated that moisture supplies for wintertime precipitation over the TP come mainly from the west (Filippi et al., 2014; Liu et al., 2017; Sun & Wang, 2014; Tian et al., 2007), Africa (Pan et al., 2018), or the Indian Ocean (An et al., 2017). By contrast, we find that most moisture for wintertime intense precipitation events over the three snowy subregions of the TP originates from the south, especially the Indian Peninsula. This discrepancy can be explained as follows. First, the cases under examination are different. Most previous studies focused on identifying moisture sources for precipitation during the whole winter season (An et al., 2017; Filippi et al., 2014; Liu et al., 2017; Pan et al., 2018; Sun & Wang, 2014; Tian et al., 2007), when the prevailing winds over the TP and its surrounding areas are westerly. By contrast, our study focuses on the moisture sources for the intense precipitation events that are more likely to result in severe snow disasters. Second, the regions under examination are different. Meteorological conditions vary substantially among different subregions over the TP. For instance, Sun and Wang (2014) focused on semiarid grasslands on the TP, while our study examines three snowy subregions along the southern periphery of the TP. Third, important details of the methodology are different. Such details may include the Lagrangian tracking software, the reanalysis products used to drive the model, the moisture source attribution methods, and the criteria used to define the moisture source regions. Our results in this study are supported by several recent studies linking wintertime intense precipitation events in and around the TP to the occurrence of western disturbances (Cannon et al., 2014, 2015, 2016; Dimri et al., 2015; Forsythe et al., 2017; Huang et al., 2018; Li et al., 2018). Southerly winds downstream of these western disturbances favor moisture transport from the south to the TP, as emphasized in our conclusions.

Acknowledgments
This work was jointly supported by the National Natural Science Foundation of China (91737307) and Tsinghua University Initiative Scientific Research Program (2019Z07L02011). The ERA-Interim reanalysis product is available from https://www.ecmwf.int/en/forecasts/datasets/reanalysis-datasets/era-interim website. The APHRODITE precipitation data are available from http://www.chikyu.ac.jp/precip/english/products.html website. The TRMM precipitation data are available from https://pmm.nasa.gov/data-access/downloads/trmm website. The GPCP precipitation data are available from http://eagle1.umd.edu/GPCP_CDR/Daily_Data website.

References

An, W., Hou, S., Zhang, Q., Zhang, W., Wu, S., Xu, H., et al. (2017). Enhanced recent local moisture recycling on the Northwestern Tibetan Plateau deduced from ice core deuterium excess records. *Journal of Geophysical Research: Atmospheres*, *122*, 12,541–12,556. https://doi.org/10.1002/2017JD027235

Bonacina, L. (1945). Orographic rainfall and its place in the hydrology of the globe. *Quarterly Journal of the Royal Meteorological Society*, *71*(307–308), 41–55. https://doi.org/10.1002/qj.49707130705

Bookhagen, B., & Burbank, D. W. (2010). Toward a complete Himalayan hydrological budget: Spatiotemporal distribution of snowmelt and rainfall and their impact on river discharge. *Journal of Geophysical Research*, *115*, F03019. https://doi.org/10.1029/2009JF001426

Cannon, F., Carvalho, L., Jones, C., & Bookhagen, B. (2014). Multi-annual variations in winter westerly disturbance activity affecting the Himalaya. *Climate Dynamics*, *44*, 441–455. https://doi.org/10.1007/s00382-014-2248-8

Cannon, F., Carvalho, L., Jones, C., Hoell, A., Norris, J., Kiladis, G., & Tahir, A. (2016). The influence of tropical forcing on extreme winter precipitation in the western Himalaya. *Climate Dynamics*, *48*, 1213. https://doi.org/10.1007/s00382-016-3137-0

Cannon, F., Carvalho, L., Jones, C., & Norris, J. (2015). Winter westerly disturbance dynamics and precipitation in the western Himalaya and Karakoram: A wave-tracking approach. *Theoretical and Applied Climatology*, *125*, 27–44. https://doi.org/10.1007/s00704-015-1489-8

Chu, D., Xie, H., Wang, P., Guo, J., La, J., Qiu, Y., & Zheng, Z. (2014). Snow cover variation over the Tibetan Plateau from MODIS and comparison with ground observations. *Journal of Applied Remote Sensing*, *8*, 084690. https://doi.org/10.1117/1.JRS.8.084690

Curio, J., Maussion, F., & Scherer, D. (2015). A 12-year high-resolution climatology of atmospheric water transport over the Tibetan Plateau. *Earth System Dynamics*, *6*, 109–124. https://doi.org/10.5194/esd-6-109-2015

Curio, J., & Scherer, D. (2016). Seasonality and spatial variability of dynamic precipitation controls on the Tibetan Plateau. *Earth System Dynamics*, *7*, 767–782. https://doi.org/10.5194/esd-7-767-2016

Dee, D. P., Uppala, S. M., Simmons, A. J., Berrisford, P., Poli, P., Kobayashi, S., et al. (2011). The ERA-Interim reanalysis: Configuration and performance of the data assimilation system. *Quarterly Journal of the Royal Meteorological Society*, *137*(656), 553–597. https://doi.org/10.1002/qj.828

Dimri, A. P., Niyogi, D., Barros, A. P., Ridley, J., Mohanty, U. C., Yasunari, T., & Sikka, D. R. (2015). Western disturbances: A review. *Reviews of Geophysics*, *53*, 225–246. https://doi.org/10.1002/2014RG000460

Filippi, L., Palazzi, E., von Hardenberg, J., & Provenzale, A. (2014). Multidecadal variations in the relationship between the NAO and winter precipitation in the Hindu Kush–Karakoram. *Journal of Climate*, *27*, 7890–7902. https://doi.org/10.1175/JCLI-D-14-00286.1

Forsythe, N., Fowler, H., Li, X., Blenkinsop, S., & Pritchard, D. (2017). Karakoram temperature and glacial melt driven by regional atmospheric circulation variability. *Nature Climate Change*, *7*, 664–670. https://doi.org/10.1038/nclimate3361

Gao, M., Qin, Z., & Xu, B. (2008). Integration of remote sensing with GIS for grassland snow cover monitoring and snow disaster evaluating in Tibet. *Proceedings of SPIE—the International Society for Optical Engineering*, *7110*, 71100O. https://doi.org/10.1117/12.800047

Guo, Y., & Wang, C. (2014). Trends in precipitation recycling over the Qinghai–Xizang Plateau in last decades. *Journal of Hydrology*, *517*, 826–835. https://doi.org/10.1016/j.jhydrol.2014.06.006

Huang, W., He, X., Yang, Z., Qiu, T., Wright, J. S., Wang, B., & Lin, D. (2018). Moisture sources for wintertime extreme precipitation events over South China during 1979–2013. *Journal of Geophysical Research: Atmospheres*, *123*, 6690–6712. https://doi.org/10.1029/2018JD028485

Huang, W., Qiu, T., Yang, Z., Lin, D., Wright, J. S., Wang, B., & He, X. (2018). On the formation mechanism for wintertime extreme precipitation events over the southeastern Tibetan Plateau. *Journal of Geophysical Research: Atmospheres*, *123*, 12,692–12,714. https://doi.org/10.1029/2018JD028921

Huffman, G. J., Adler, R. F., Bolvin, D. T., Gu, G., Nelkin, E. J., Bowman, K. P., et al. (2007). The TRMM Multisatellite Precipitation Analysis (TMPA): Quasi-Global, Multiyear, Combined-Sensor Precipitation Estimates at Fine Scales. *Journal of Hydrometeorology*, *8*, 38–55. https://doi.org/10.1175/JHM560.1

Huffman, G. J., Adler, R. F., Morrissey, M. M., Bolvin, D. T., Curtis, S., Joyce, R., et al. (2001). Global precipitation at one-degree daily resolution from multisatellite observations. *Journal of Hydrometeorology*, *2*(1), 36–50. https://doi.org/10.1175/1525-7541(2001)002<0036:GPAODD>2.0.CO;2

Immerzeel, W., Beek, L., & Bierkens, M. (2010). Climate change will affect the Asian water towers. *Science*, *328*(5984), 1382–1385. https://doi.org/10.1126/science.1183188

James, P., Stohl, A., Spichtinger, N., Eckhardt, S., & Forster, C. (2004). Climatological aspects of the extreme European rainfall of August 2002 and a trajectory method for estimating the associated evaporative source regions. *Natural Hazards and Earth System Sciences*, *4*, 733–746. https://doi.org/10.5194/nhess-4-733-2004

Kitoh, A., & Arakawa, O. (2016). Reduction in the east-west contrast in water budget over the Tibetan Plateau under a future climate. *Hydrological Research Letters*, *10*, 113–118. https://doi.org/10.3178/hrl.10.113

Kulkarni, A., Mathur, P., Rathore, B., Alex, S., Thakur, N., & Kumar, M. (2002). Effect of global warming on snow ablation pattern in the Himalaya. *Current Science*, *83*(2), 120–123.

Kurosaki, Y., & Kimura, F. (2002). Relationship between topography and daytime cloud activity around Tibetan Plateau. *Journal of the Meteorological Society of Japan*, *80*, 1339–1355. https://doi.org/10.2151/jmsj.80.1339

Lang, T., & Barros, A. (2004). Winter storms in the Central Himalayas. *Journal of the Meteorological Society of Japan*, *82*, 829–844. https://doi.org/10.2151/jmsj.2004.829

Li, X., Fowler, H. J., Forsythe, N., Blenkinsop, S., & Pritchard, D. (2018). The Karakoram/Western Tibetan vortex: Seasonal and year-to-year variability. *Climate Dynamics*, *51*, 3883–3906. https://doi.org/10.1007/s00382-018-4118-2

Li, C., Su, F., Yang, D., Tong, K., Meng, F., & Kan, B. (2017). Spatiotemporal variation of snow cover over the Tibetan Plateau based on MODIS snow product, 2001–2014. *International Journal of Climatology*, *38*, 708–728. https://doi.org/10.1002/joc.5204

Li, Y., Ye, T., Liu, W., & Gao, Y. (2018). Linking livestock snow disaster mortality and environmental stressors in the Qinghai-Tibetan Plateau: Quantification based on generalized additive models. *Science of The Total Environment*, *625*, 87–95. https://doi.org/10.1016/j.scitotenv.2017.12.230

Liu, H., Liu, X., & Dong, B. (2017). Intraseasonal variability of winter precipitation over Central Asia and the Western Tibetan Plateau from 1979 to 2013 and its relationship with the North Atlantic Oscillation. *Dynamics of Atmospheres and Oceans*, *79*, 31–42. https://doi.org/10.1016/j.dynatmoce.2017.07.001

Liu, F., Mao, X., Zhang, Y., Chen, Q., Liu, P., & Zhao, Z. (2014). Risk analysis of snow disaster in the pastoral areas of the Qinghai-Tibet Plateau. *Journal of Geographical Sciences*, *24*(3), 411–426. https://doi.org/10.1007/s11442-014-1097-z

Liu, W., Wang, L., Chen, D., Tu, K., Ruan, C., & Hu, Z. (2016). Large-scale circulation classification and its links to observed precipitation in the eastern and central Tibetan Plateau. *Climate Dynamics*, *46*(11), 3481–3497. https://doi.org/10.1007/s00382-015-2782-z

Lu, C., Yu, G., & Xie, G. (2005). Tibetan Plateau serves as a water tower. *International Geoscience and Remote Sensing Symposium*, *5*, 3120–3123. https://doi.org/10.1109/IGARSS.2005.1526498

Madonna, E., Wernli, H., Joos, H., & Martius, O. (2014). Warm Conveyor Belts in the ERA-Interim Dataset (1979–2010). Part I: Climatology and Potential Vorticity Evolution. *Journal of Climate*, *27*, 3–26. https://doi.org/10.1175/JCLI-D-12-00720.1

Martius, O., Sodemann, H., Joos, H., Pfahl, S., Winschall, A., Croci-Maspoli, M., et al. (2013). The role of upper-level dynamics and surface processes for the Pakistan flood of July 2010. *Quarterly Journal of the Royal Meteorological Society*, *139*(676), 1780–1797. https://doi.org/10.1002/qj.2082

Masafumi, H., & Kenji, N. (2005). Spatial and diurnal variation of precipitation systems over Asia observed by the TRMM Precipitation Radar. *Journal of Geophysical Research*, *110*, D05106. https://doi.org/10.1029/2004JD004815

Maussion, F., Scherer, D., Mölg, T., Collier, E., Curio, J., & Finkelnburg, R. (2014). Precipitation seasonality and variability over the Tibetan Plateau as resolved by the high Asia reanalysis. *Journal of Climate*, *27*(5), 1910–1927. https://doi.org/10.1175/JCLI-D-13-00282.1

Palazzi, E., von Hardenberg, J., & Provenzale, A. (2013). Precipitation in the Hindu-Kush Karakoram Himalaya: Observations and future scenarios. *Journal of Geophysical Research: Atmospheres*, *118*, 85–100. https://doi.org/10.1029/2012JD018697

Pan, C., Zhu, B., Gao, J., Kang, H., & Zhu, T. (2018). Quantitative identification of moisture sources over the Tibetan Plateau and the relationship between thermal forcing and moisture transport. *Climate Dynamics*, *52*, 181. https://doi.org/10.1007/s00382-018-4130-6

Pfahl, S., Madonna, E., Boettcher, M., Joos, H., & Wernli, H. (2014). Warm conveyor belts in the ERA-Interim dataset (1979–2010). Part II: Moisture origin and relevance for precipitation. *Journal of Climate*, *27*, 27–40. https://doi.org/10.1175/JCLI-D-13-00223.1

Pu, Z., & Xu, L. (2009). MODIS/Terra observed snow cover over the Tibet Plateau: Distribution, variation and possible connection with the East Asian Summer Monsoon (EASM). *Theoretical and Applied Climatology*, *97*(3), 265–278. https://doi.org/10.1007/s00704-008-0074-9

Pu, Z., Xu, L., & Salomonson, V. (2007). MODIS/Terra observed seasonal variations of snow cover over the Tibetan Plateau. *Geophysical Research Letters*, *34*, L06706. https://doi.org/10.1029/2007GL029262

Qin, D., Liu, S., & Li, P. (2006). Snow cover distribution, variability, and response to climate change in Western China. *Journal of Climate*, *19*(9), 1820–1833. https://doi.org/10.1175/JCLI3694.1

Qiu, J. (2008). China: The third pole. *Nature*, *454*, 393–396. https://doi.org/10.1038/454393a

Qiu, X., Yang, X., Fang, Y., Xu, Y., & Zhu, F. (2018). Impacts of snow disaster on rural livelihoods in southern Tibet-Qinghai Plateau. *International Journal of Disaster Risk Reduction*, *31*, 143–152. https://doi.org/10.1016/j.ijdrr.2018.05.007

Shafiq, M., Rasool, R., Ahmed, P., & Dimri, A. P. (2018). Temperature and precipitation trends in Kashmir Valley, north western Himalayas. *Theoretical and Applied Climatology*, *135*, 293–304. https://doi.org/10.1007/s00704-018-2377-9

Shen, S. S., Yao, R., Ngo, J., Basist, A. M., Thomas, N., & Yao, T. (2015). Characteristics of the Tibetan Plateau snow cover variations based on daily data during 1997–2011. *Theoretical and Applied Climatology*, *120*(3), 445–453. https://doi.org/10.1007/s00704-014-1185-0

Smith, T., & Bookhagen, B. (2018). Changes in seasonal snow water equivalent distribution in High Mountain Asia (1987 to 2009). *Science Advances*, *4*(1), e1701550. https://doi.org/10.1126/sciadv.1701550

Sodemann, H., Schwierz, C., & Wernli, H. (2008). Interannual variability of Greenland winter precipitation sources: Lagrangian moisture diagnostic and North Atlantic Oscillation influence. *Journal of Geophysical Research*, *113*, D03107. https://doi.org/10.1029/2007JD008503

Sprenger, M., & Wernli, H. (2015). The LAGRANTO Lagrangian analysis tool—Version 2.0. *Geoscientific Model Development*, *8*(8), 2569–2586. https://doi.org/10.5194/gmd-8-2569-2015

Stohl, A., & James, P. (2004). A Lagrangian analysis of the atmospheric branch of the Global Water Cycle. Part I: Method description, validation, and demonstration for the August 2002 flooding in central Europe. *Journal of Hydrometeorology*, *5*(4), 656–678. https://doi.org/10.1175/1525-7541(2004)005<0656:ALAOTA>2.0.CO;2

Su, F., Duan, X., Chen, D., Hao, Z., & Cuo, L. (2013). Evaluation of the Global Climate Models in the CMIP5 over the Tibetan Plateau. *Journal of Climate*, *26*, 3187–3208. https://doi.org/10.1175/JCLI-D-12-00321.1

Sun, B., & Wang, H. (2014). Moisture sources of semiarid grassland in China using the Lagrangian particle model FLEXPART. *Journal of Climate*, *27*, 2457–2474. https://doi.org/10.1175/JCLI-D-13-00517.1

Syed, F., Giorgi, F., Pal, J., & King, M. P. (2006). Effect of remote forcings on the winter precipitation of central southwest Asia part 1: Observations. *Theoretical and Applied Climatology*, *86*, 147–160. https://doi.org/10.1007/s00704-005-0217-1

Tang, G., Long, D., Hong, Y., Gao, J., & Wan, W. (2018). Documentation of multifactorial relationships between precipitation and topography of the Tibetan Plateau using spaceborne precipitation radars. *Remote Sensing of Environment*, *208*, 82–96. https://doi.org/10.1016/j.rse.2018.02.007

Tian, L., Yao, T., MacClune, K., White, J. W. C., Schilla, A., Vaughn, B., et al. (2007). Stable isotopic variations in west China: A consideration of moisture sources. *Journal of Geophysical Research*, *112*, D10112. https://doi.org/10.1029/2006JD007718

Tiwari, S., Kar, S. C., & Bhatla, R. (2017). Atmospheric moisture budget during winter seasons in the western Himalayan region. *Climate Dynamics*, *48*(3–4), 1277–1295. https://doi.org/10.1007/s00382-016-3141-4

Tong, K., Su, F., Yang, D., Zhang, L., & Hao, Z. (2014). Tibetan Plateau precipitation as depicted by gauge observations, reanalyses and satellite retrievals. *International Journal of Climatology*, *34*, 265–285. https://doi.org/10.1002/joc.3682

Trenberth, K. E. (1998). Atmospheric moisture residence times and cycling: Implications for rainfall rates and climate change. *Climatic Change*, *39*(4), 667–694. https://doi.org/10.1023/A:1005319109110

Trenberth, K. E. (1999). Atmospheric moisture recycling: Role of advection and local evaporation. *Journal of Climate*, *12*(5), 1368–1381. https://doi.org/10.1175/1520-0442(1999)012<1368:AMRROA>2.0.CO;2

Tucker, D. (2005). Orographic precipitation, *Encyclopedia of World Climatology* (pp. 552–555). Dordrecht: Springer. https://doi.org/10.1007/1-4020-3266-8&urluscore;153

Wan, G., Yang, M., Liu, Z., Wang, X., & Liang, X. (2017). The precipitation variations in the Qinghai-Xizang (Tibetan) Plateau during 1961–2015. *Atmosphere*, *8*, 80. https://doi.org/10.3390/atmos8050080

Wang, X., Pang, G., & Yang, M. (2018). Precipitation over the Tibetan Plateau during recent decades: A review based on observations and simulations. *International Journal of Climatology*, *38*(3), 1116–1131. https://doi.org/10.1002/joc.5246

Wang, X., Wu, C., Wang, H., Gonsamo, A., & Liu, Z. (2017). No evidence of widespread decline of snow cover on the Tibetan Plateau over 2000–2015. *Scientific Reports*, *7*(1), 14645. https://doi.org/10.1038/s41598-017-15208-9

Wernli, H., & Davies, H. C. (1997). A Lagrangian-based analysis of extratropical cyclones. I: The method and some applications. *Quarterly Journal of the Royal Meteorological Society*, *123*(538), 467–489. https://doi.org/10.1002/qj.49712353811

Xu, X., Lu, C., Shi, X., & Gao, S. (2008). World water tower: An atmospheric perspective. *Geophysical Research Letters*, *35*, L20815. https://doi.org/10.1029/2008GL035867

Yao, T., Thompson, L., Yang, W., Yu, W., Gao, Y., Guo, X., et al. (2012). Different glacier status with atmospheric circulations in Tibetan Plateau and surroundings. *Nature Climate Change*, *2*, 663–667. https://doi.org/10.1038/nclimate1580

Yatagai, A., Arakawa, O., Kamiguchi, K., Kawamoto, H., Nodzu, M., & Hamada, A. (2009). A 44-year daily gridded precipitation dataset for Asia based on a dense network of rain gauges. *SOLA*, *5*, 137–140. https://doi.org/10.2151/sola.2009-035

Yin, H., Cao, C., Xu, M., Chen, W., Ni, X., & Chen, X. (2017). Long-term snow disasters during 1982–2012 in the Tibetan Plateau using satellite data. *Geomatics Natural Hazards and Risk*, *8*(2), 466–477. https://doi.org/10.1080/19475705.2016.1238851